


## ORIGINAL RESEARCH

# Laboratory multistatic 3D SAR with polarimetry and sparse aperture sampling

Richard Welsh<sup>1</sup>  | Daniel Andre<sup>1</sup>  | Mark Finnis<sup>2</sup>
<sup>1</sup>Centre for Electronic Warfare, Information and Cyber, Cranfield University, Defence Academy of the United Kingdom, Shrivenham, UK

<sup>2</sup>Centre for Defence Engineering, Cranfield University, Defence Academy of the United Kingdom, Shrivenham, UK

## Correspondence

Daniel Andre.

Email: [d.andre@cranfield.ac.uk](mailto:d.andre@cranfield.ac.uk)

## Funding information

Defence Science and Technology Laboratory,  
Grant/Award Number: P15684

## Abstract

With the advent of constellations of SAR satellites, and the possibility of swarms of SAR UAV's, there is increased interest in multistatic SAR image formation. This may provide advantages including allowing three-dimensional image formation free of clutter overlay; the coherent combination of bistatic SAR geometries for improved image resolution; and the collection of additional scattering information, including polarimetric. The polarimetric collection may provide useful target information, such as its orientation, polarisability, or number of interactions with the radar signal; distributed receivers would be more likely to capture any bright specular responses from targets in the scene, making target outlines distinct. Highlight results from multistatic polarimetric SAR experiments at the Cranfield University GBSAR laboratory are presented, illustrating the utility of the approach for fully sampled 3D SAR image formation, and for sparse aperture SAR 3D point-cloud generation with a newly developed volumetric multistatic interferometry algorithm.

## KEYWORDS

height measurement, multistatic radar, polarisation, radar interferometry, synthetic aperture radar

## 1 | INTRODUCTION

With the advent of constellations of Synthetic Aperture Radar (SAR) satellites, and the possibility of swarms of SAR Unmanned Aerial Vehicles (UAV)'s [1, 2], there is increased interest in multistatic SAR image formation.

These types of collections may provide advantages including allowing three-dimensional (3D) image formation free of clutter overlay; the coherent combination of bistatic SAR geometry collections for improved image resolution; the collection of additional scattering information, including polarimetric.

Polarimetric collections allow for more scene data to be collected and may provide additional target information, such as scatterer orientation, polarisability, or number of interactions with the radar signal [3–5]. Furthermore, distributed receivers would be more likely to capture any bright specular responses from targets in the scene, making target outlines distinct.

Obtaining 3D SAR imagery is desirable for object recognition, though providing sufficient SAR aperture sampling in the vertical dimension can be challenging. Hence there is a need for the development of new image formation algorithms that only require sparsely sampled apertures [6, 7].

Several approaches to forming 3D SAR scene renderings from sparsely sampled collections have been developed. These include dual-pass SAR interferometry, 3D SAR compressive sensing and the SAR Point-Cloud Generation System (SPCGS) [8–10]. Dual-pass SAR interferometry is used to construct Digital Elevation Models (DEMs) of target scenes and can involve phase unwrapping methods. This method often struggles with manmade targets due to scene height discontinuities which can give rise to several scatterers of different height being overlaid. The approach developed for the SPCGS estimates 3D locations of scatterers by summing the phase factors from a series of 2D SAR interferograms collected with a sparse set of elevation angles. This method utilises the change in layover within a stack of 2D images, with the assumption

This is an open access article under the terms of the [Creative Commons Attribution](https://creativecommons.org/licenses/by/4.0/) License, which permits use, distribution and reproduction in any medium, provided the original work is properly cited.

© 2024 The Authors. *IET Radar, Sonar & Navigation* published by John Wiley & Sons Ltd on behalf of The Institution of Engineering and Technology.

that the SAR collections are monostatic, are in a far-field scenario, and have constant grazing angle across the scene. The approach has been successful in forming target renderings from simulated monostatic datasets [11]. However, the assumptions made for this approach would not generally hold true for data collected with SAR satellite constellations and UAV-SAR drone swarms. This is due to their use of multiple receiver locations being significantly separated from that of the transmitter. Processing these collection geometries can introduce distortions to the SAR scatterer layover due to their asymmetrical nature [12, 13].

Sparse reconstruction methods, such as compressive sensing, have been the focus of recent tomographic SAR research. This approach has mainly achieved success in areas such as urban mapping. Such scenarios can be relied upon for having largely empty scenes, which is exploited in the sparse reconstruction approach [14]. The application to vehicle targets has been limited thus far, with simple 3D renderings being produced of model tanks [15]. Applying this technique to sparse 3D swarm sensing may be complicated by the need to estimate scatterer reflectivity for multiple bistatic angles, although simulated 3D renderings have been formed [16].

Results from multistatic polarimetric SAR experiments at the Cranfield University GBSAR laboratory [17] are presented, illustrating the utility of the approach for fully sampled 3D SAR image formation, and for sparse aperture sampled SAR 3D point-cloud generation.

Bistatic geometries give rise to non-trivial polarimetric scattering, so that for example, linear cross-polarisations are not equal, Section 2 describes a polarimetric decomposition promising for interpretation of multistatic scattering.

Section 3 describes the extension of a newly developed 3D point-cloud algorithm which operates with multistatic geometries apertures and is valid in the most general SAR near-field multistatic geometries. The use of all linear polarisation channels is also considered.

Section 4 describes the laboratory SAR measurements undertaken. The simulations in Section 5 present the workings of the sparse 3D aperture approach, defining parameters that would enable multistatic trajectories to be designed for an optimal performance of the new approach. Section 6 presents fully sampled 2D SAR aperture results whilst Section 7 presents sparsely sampled SAR aperture 3D point-cloud results, for each measured polarisation channel. Concluding remarks are presented in Section 8.

## 2 | BISTATIC POLARIMETRIC DECOMPOSITION

Monostatic polarimetric decompositions and their physical interpretation are well understood. However, the physical interpretation of various decomposition generalizations to the bistatic case are not so well understood. Some bistatic decomposition approaches are only slight modifications of existing monostatic approaches, for example, simply introducing an anti-symmetric component to the target scattering

matrix (which is always symmetric in the monostatic case). However, the physical meaning associated with this polarimetric parameter extraction may be unclear, and increasingly so where the geometry is far from the monostatic case.

The approach selected for application in this work, is that described by Titin-Schnaider [3–5] constituting a bistatic generalisation of the Huynen Fork parameter decomposition [18], providing six polarimetric parameters: for the bistatic case there are two Orientation angles and two Symmetry angles associated with the incident and scattered ray directions. The formalism has been related to a generalisation of the Cloude-Pottier parameters [4].

The bistatic generalisation of the Huynen Fork target parameters was found to provide a physically meaningful pixel based polarimetric decomposition [5]. In the monostatic case there are four parameters of interest  $\theta \tau \nu \gamma$  (theta, tau, nu, gamma) representing:

- **Orientation/Tilt angle,  $\theta$ :** linked to the angle between the projection of the scatterer main axis and the horizontal reference angle:  $-90^\circ \leq \theta \leq 90^\circ$ . Here we define a positive rotation as clockwise about the down-range direction. Scatterers for which the tilt angle may be meaningful include rods/dipoles and straight edges of extended objects.
- **Symmetry angle,  $\tau$ :** allowing the separation of symmetric and non-symmetric scatterers. A symmetric scatterer is symmetric about a plane containing the incident ray,  $0^\circ \leq |\tau| \leq 45^\circ$ , where  $0^\circ$  indicates high symmetry, and  $|\tau| = 45^\circ$  indicates low symmetry. Scatterers with high symmetry would include spheres, rods/dipoles and corner reflectors.
- **Skip angle,  $\nu$ :** divides scatterers into two classes according, approximately, to whether the scattered rays have had an odd or even number of bounces:  $0^\circ \leq |\nu| \leq 45^\circ$ , where  $0^\circ$  indicates an Odd-bounce interaction and  $|\nu| = 45^\circ$  indicates an Even-bounce interaction. Odd-bounce scatterers include spheres, flat plates and trihedral multi-bounce. Even-bounce scatterers include dihedral multi-bounce. Note that at certain aspects the dihedral response may be dominated by single flat plate responses or straight edge diffraction.
- **Polarisability angle,  $\gamma$ :** in this approach is taken to mean that the scatterer only returns waves with a particular polarization regardless of incident polarization, hence a polarization projection:  $0^\circ \leq \gamma \leq 45^\circ$ , where  $0^\circ$  indicates high polarisability and  $45^\circ$  low. Scatterers with medium to high polarisability include rods and the straight edges of extended objects. Scatterers with low polarisability include spheres, flat plates, and corner reflectors with multi-bounce including both dihedrals and trihedrals.

For the bistatic case there are two  $\tau$  parameters,  $\tau_i \tau_s$ , and two  $\theta$  parameters,  $\theta_i \theta_s$ , where “i” stands for the incident direction, and “s” for the scattered direction. In the monostatic case these directions are equivalent, so that the  $\tau$  values become the same, and the  $\theta$  values become the same. It is noted that once the orientation parameters are determined ( $\theta_i, \theta_s$ ), the additional Huynen parameters provide information

intrinsic to the electro-magnetic mechanism itself, that is, they are independent of input and output antenna orientations.

### 3 | SPARSE APERTURE 3D POINT-CLOUD ALGORITHM

A new sparse SAR aperture imaging approach, Sparse SAR Volumetric Interferometry (SSARVI) is described here. It is a generalisation of the SPCGS algorithm, in this case applicable to multistatic and SAR near-field imaged scenes. Previously the performance of the algorithm was demonstrated for monostatic and bistatic scenarios for a single polarisation channel [19], whereas here it is demonstrated on multistatic collections. It exploits the benefits of volumetric processing, allowing laid over scatterers to be processed and distinguished in a natural manner [20]. A wide variety of multistatic SAR geometry scenarios can be accommodated by the algorithm, however in the results presented here, multiple simultaneous fixed receiver positions are used, together with multiple horizontal passes of the transmitter at different heights. It is noted that a randomised trajectory spacing in height suppresses vertical aliasing artefacts [10, 11]. In the multistatic scenario, this randomised spacing should be imparted to Bistatic Equivalent Monostatic (BEM) trajectories which follow the bistatic bisectors of the corresponding transceiver locations. This new approach does not require the intensive signal reconstruction processes, or phase unwrapping, used for other sparse 3D SAR techniques [21].

Within a multistatic collection, having chosen the reference bistatic collection, the other bistatic collections can then be combined with the reference to form volumetric interferograms. Each volumetric interferogram contributes vertical SAR iso-range arcs at the scatterer locations (with no vertical resolution themselves), but when combining different interferograms, the arcs cross at the scatterer 3D location, allowing the scatterer heights to be determined by the locations of maximum interferogram phase factor sum, to be introduced next.

Considering  $N$  bistatic SAR geometry collections (comprising the multistatic SAR collection), the sum of the interferogram phase factors is evaluated at each voxel location:

$$R(\mathbf{x}) = \frac{1}{N} \left| 1 + \sum_{n=1}^{N-1} e^{i\varphi_n(\mathbf{x})} \right| \quad (1)$$

where  $\varphi_n(\mathbf{x})$  is the phase at voxel  $\mathbf{x}$  of the  $n$ th interferogram. Voxel locations where the summed phase  $R$  has surpassed a designated threshold, form part of a point-cloud rendering of the target being imaged. Detections are determined by the use of a threshold, which can be implemented through histogram-based approaches that are common in image processing [22]. The point-clouds can then be augmented by associating the mean voxel intensity of the contributing SAR data, at the position of each individual point detection. The multistatic extension of the SSARVI approach is summarised by the flow diagram in Figure 1.

Many approaches to combining SAR data from contributing bistatic geometries are possible, however three approaches are here employed, attuned to the particular SAR measurements undertaken in the laboratory. The three approaches may offer benefits in the case of complex targets, to be commented on below. The effect on performance of each method of combination is considered both theoretically and experimentally. This is due to the improvement in resolution associated with multistatic geometries, but also the challenges of combining multiple received signals. The main challenges arise from varying signal returns from complex volumetric targets over a wide baseline and signal co-registration [23–26].

Let there be  $N$  transmitter passes undertaken, with  $M$  receivers. For the  $m$ th receiver, the sum of interferometric phase factors corresponding to the  $N$  transmitter passes,  $R_m(\mathbf{x})$ , is obtained via Equation (1). The three approaches to multistatic point-cloud generation used are:

1. **Coherent multistatic sum:** a coherent combination of all  $N-1$  interferograms for all transmitter (Tx) and receiver (Rx) combinations, with the threshold being applied to the absolute value of the phase factor sum:

$$\text{Det} = \frac{1}{M} \left| \sum_{m=1}^M R_m(\mathbf{x}) \right| > Th \quad (2)$$

where Det is the set of point-cloud detections and  $Th$  is the threshold derived from the histogram-based approach. For omnidirectional point scatterers, this could offer finer resolution than other approaches, however it could prove overly sensitive when applied to variable bistatic RCS scatterers.

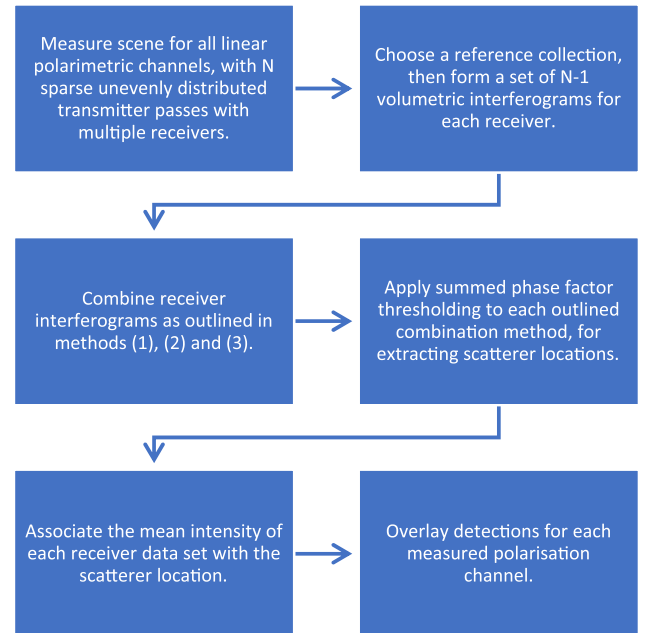


**FIGURE 1** Flow diagram of the multistatic and polarimetric extension to the SSARVI algorithm.

2. **Non-coherent bistatic sum:** a coherent sum of all the bistatic geometry interferograms corresponding to each receiver trajectory, and then an absolute value sum of these values:

$$\text{Det} = \frac{1}{M} \sum_{m=1}^M |R_m(\mathbf{x})| > Th \quad (3)$$

Where the threshold is applied to the final sum. This approach could offer greater stability to complex target RCS variation than the fully coherent summation approach, when applied to experimental data.

3. **Non-coherent bistatic combination:** a combination of the detections obtained from each receiver - a threshold is applied separately to the coherent summed interferograms corresponding to each receiver, and these detections are combined:

$$\text{Det} = \bigcup_{m=1}^M \text{Det}_m, \quad (4)$$

where  $\text{Det}_m = R_m(\mathbf{x}) > Th_m$

This approach may be most robust to variation in scatterer RCS from complex targets, however, of the three methods this approach would offer the least multistatic based spatial resolution improvement.

The performance of each of these methods is demonstrated on a simulated isotropic point scatterer and on multi-polarisation experimental data from a complex target measurement.

## 4 | LABORATORY MEASUREMENTS

The GBSAR laboratory conducts microwave measurements with a Vector Network Analyser (VNA), which generates a stepped frequency waveform. The system was set up for indoor use, with two Ultra-Wideband horn antennas allowing measurements within the range 1–10 GHz. The Antennae can be mounted in a bistatic or pseudo monostatic configuration.

When in a bistatic configuration, seen in Figure 2, each antenna is mounted on a different two-dimensional vertical SAR aperture scanner. One SAR aperture was 3.50 m wide by 1.46 m high and was used for the transmitter, and the other was 1.29 m wide by 1.46 m high and was used for the receiver, as seen in Figure 3.

When a SAR scene is left undisturbed, and transmitter trajectories are precisely repeated, the combination of repeat scans with the receiver in different locations (or trajectories) are equivalent to a multistatic scan with multiple receivers operating simultaneously. Using this approach, multistatic scans have been collected in the GBSAR lab, even though the VNA has only two ports.

The multistatic SAR geometry chosen for this collection is shown in Figure 2. The transmitter traverses the vertical rectangular aperture in blue, with Nyquist positional sampling, and nine fixed receiver positions to the left of the scene, numbered 1-9 in the figure, provide nine bistatic 3D SAR

collections. For sparse aperture image analysis, the collected dataset is downsampled.

The measured target scene for the results presented, consisted of a quarter scale T72 tank model placed on gravel and reference spheres, seen in Figure 4. The gravel provides a speckle background, with target shadowing visible depending on SAR geometry. The use of a stationary target allows for optimal algorithm development.

## 5 | SIMULATIONS

### 5.1 | Introduction

To explore the performance of the SSARVI algorithm for multistatic SAR collections, simulations of a single point scatterer were conducted and are described in this section.



FIGURE 2 The GBSAR laboratory in a bistatic configuration.

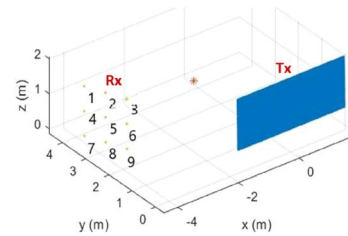


FIGURE 3 Multistatic 3D SAR geometry, with 2D SAR aperture transmitter trajectory in blue, and nine fixed receiver positions to the left of the scene.



FIGURE 4 Target scene, consisting of a Quarter scale T72 tank model on gravel and reference sphere “S”.

Previously it was found that randomized spacing trajectory distributions in height with a normalised trajectory spacing standard deviation (NSTD) of approximately 0.6 gave the best peak to sidelobe performance [19]. However, for higher NSTD values the peak to sidelobe performance was seen to drop again. It was hypothesised that this drop was due to the clustering of trajectories that occurs for higher NSTD values. In this section we therefore investigate how trajectory clustering affects peak to sidelobe levels. In these simulations, for  $N$  transmitter trajectories, the clustering is performed only on the 2nd to  $(N-1)$ th passes, which we call the mid-aperture trajectories (of which there are  $N-2$ ), leaving the top-most and end-most passes unchanged as these define the overall aperture extent.

## 5.2 | Multistatic summation approaches

For an initial simulation, the SAR geometry consisted of five transmitter height horizontal pass trajectories traversed sequentially, with three fixed position receivers at different heights operating simultaneously, seen in Figure 5. The geometry is comparable to a subset of the measurement geometry seen in Figure 3. The Bistatic-Equivalent Monostatic (BEM) passes contributed by each transmitter and receiver pair are shown in the figure – for each receiver they are coloured yellow, green, and magenta respectively. The frequency range was 7 – 8 GHz. Note that BEM antenna positions are in the bistatic direction (bisection of antenna directions from the scene centre), and at a range which is the same as the bistatic range.

The vertical extent of the transmitter aperture was 1.28 m, with heights {0.63, 0.19, -0.01, -0.21, -0.65} m, with the three fixed receiver positions offset to the right at mean bistatic angle of  $5.7^\circ$ . This combination gave a mean slant range of 6.8 m to the target. For an image unambiguous vertical cross-range of 1 m, the transmitter pass vertical spacing required is  $2.46^\circ$  in elevation. However, starting from even spacing, the second and fourth transmitter passes were here offset by  $0.38^\circ$  in elevation towards the mid-aperture, which had the effect of suppressing aliasing artefacts over the vertical cross-range extent.

The simulation results presented in Figure 6 show height estimates for the scatterer in the form of the interferometric phase factor sum value,  $R$ . The  $R$  values plotted are extracted along a vertical iso-range arc through the point scatterer, thus showing vertical sidelobe structures resulting from different transceiver aperture distributions in height.

Figure 6 shows  $R$  values for coherent and non-coherent bistatic interferogram sums corresponding to the three receiver geometries shown in Figure 5. The peak of  $R$  represents the estimate of the scatterer height in the SSARVI calculation process, and is correctly collocated with the scatterer height, at 0.4 m. Both summation methods show the suppression of ambiguities, with the sidelobe heights being significantly lower than the main peak at the scatterer position. For the given geometry, the coherent summation of

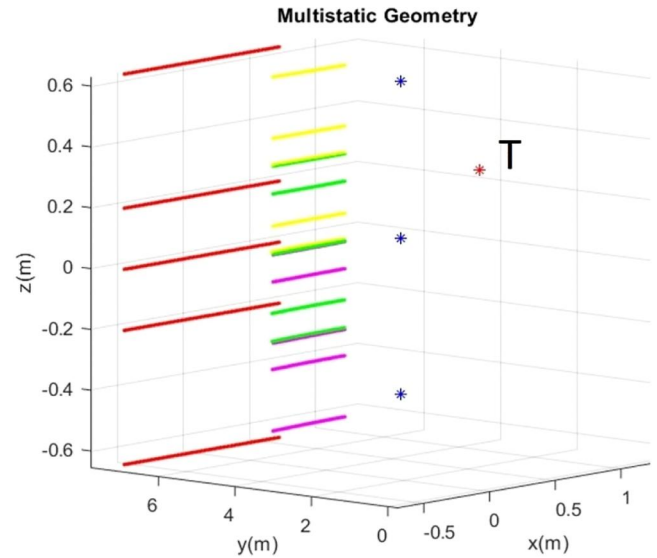


**FIGURE 5** Simulation multistatic SAR geometry with five sequential transmitter passes (red) and three simultaneous receivers (blue). The simulated point scatterer location is labelled “T”. The Bistatic Equivalent Monostatic (BEM) trajectories are also shown (yellow, green and magenta for each of the three receivers).

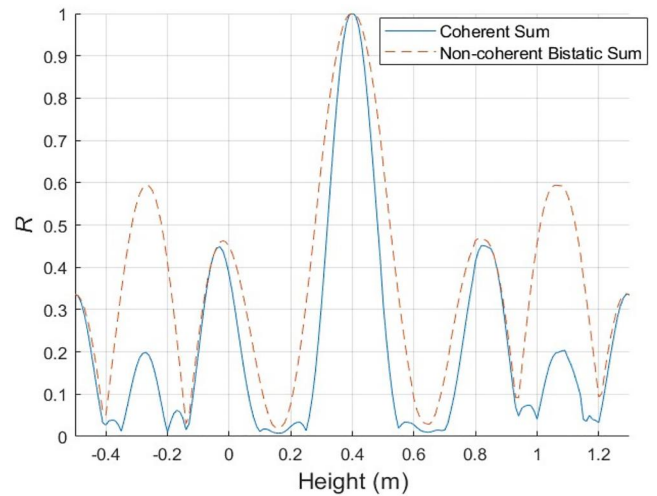


**FIGURE 6** Simulation values of summed phase factor,  $R$ , along a vertical iso-range arc from multistatic SAR simulations on a point scatterer. The performance is shown for both coherent interferogram summation from multiple receivers, and the non-coherent summed bistatic interferogram approach.

interferograms across receivers shows the greatest suppression of sidelobes, when compared to the non-coherent sum.

## 5.3 | Trajectory clustering effects

The  $R$  sidelobe height gives rise to false detections in the SSARVI algorithm, which can be influenced by the number of passes and the unevenness of the spacing between them. It has been found that generally, but only to an extent, greater unevenness in trajectory height sampling leads to greater sidelobe

suppression [19]. However, it is thought that when the unevenness is taken to the extreme within a fixed extent, passes can cluster together, effectively reducing the trajectory sampling, which is prejudicial to  $R$  sidelobe suppression. The clustering effect is investigated here.

Multiple simulations were conducted, using a generalised bistatic aperture using the mid receiver position shown in Figure 5, and with the same isotropic point-target. The transmitter passes were varied from evenly distributed, to a centrally clustered distribution as described in Section 5.1, with top and bottom passes defining the constant extent of the transmitter aperture, and the mid-aperture cluster between them.

For multiple simulations as described above, Figure 7 presents the peak to sidelobe level,  $\Delta R$ , as a function of the cluster width, for  $N$  transmitter passes. The degree of clustering is here given by the BEM (mid-aperture) cluster extent in degrees, which we denote this by  $\chi$ . Smaller values of  $\chi$  therefore represent a higher degree of clustering. The curves in the figure correspond to 6, 8, and 10 transmitter passes, and show the evolution of  $\Delta R$  with  $\chi$ , starting from an evenly sampled in height transmitter aperture. The transmitter mid-aperture passes were sequentially displaced towards the middle of the aperture, keeping the very top and very bottom passes unchanged. For the 6-pass case, the initial sampling rate matches the Nyquist sampling rate for a 1 m unambiguous vertical cross-range extent. Considering the separation of BEM passes, this corresponded to a spacing angular extent of  $0.98^\circ$ .

It is noted that the 1 m unambiguous vertical cross-range extent is especially significant, as this gives the extent over which sidelobe levels are considered in the evaluations of  $\Delta R$ , hence the  $0.98^\circ$  value is marked in the figure with a vertical dashed line and is denoted  $\chi_1$ .

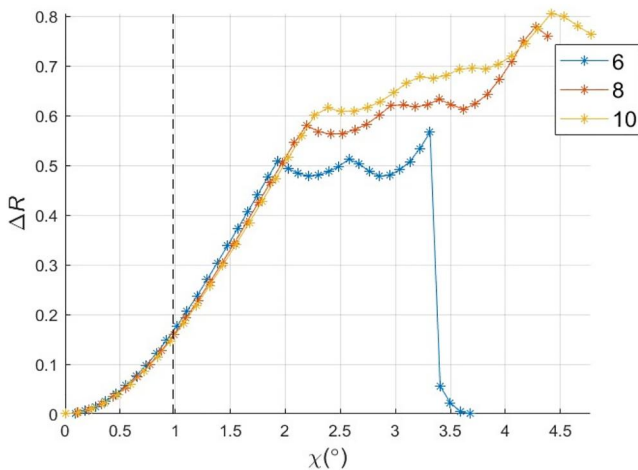


**FIGURE 7** Simulation results for  $\Delta R$  determining the relationship between the sidelobe height and the vertical aperture distribution in the form of the cluster BEM angular extent  $\chi$ . Results are shown for simulations of 6, 8, and 10 transmitter passes. The vertical dashed line indicates the angular extent corresponding to the Nyquist spacing for the 1 m unambiguous vertical cross-range extent of interest over which  $\Delta R$  is evaluated.

The three curves in Figure 7 initially behave in the same way with increasing  $\chi$ : when  $\chi$  is small,  $\Delta R$  starts at zero and progressively increases until  $\chi$  is approximately double  $\chi_1$ . This behaviour is associated with the cluster initially behaving as a single pass, so that there are effectively three passes in total, giving rise to a small unambiguous cross-range extent and poor  $\Delta R$  performance.

For  $\chi$  greater than about  $2\chi_1$ ,  $\Delta R$  performance increase is reduced and attains a maximum, where the greater the number of passes, the greater the maximum. For 10 passes,  $\Delta R$  attains 0.88.

Hence, it has been shown with an example simulation that excessive trajectory clustering can reduce the sidelobe performance substantially, due to multiple trajectories behaving as a single trajectory. In the example it is shown that for a given desired unambiguous vertical cross-range extent, the extent of clustered trajectories should not be finer than approximately two times the corresponding Nyquist sample spacing, otherwise the trajectory distribution becomes sub-optimal.

## 6 | FULL APERTURE 3D SAR IMAGE RESULTS

### 6.1 | Multistatic data summation

A multistatic polarimetric laboratory collection was performed, providing thirty-six bistatic 2D SAR aperture scans: nine bistatic scans, for each of four linear polarization channels. With this data, thirty-six 3D volumetric bistatic SAR image results were generated with the bistatic Backprojection SAR image formation algorithm (BPA).

An incoherent sum of the nine bistatic 3D SAR image VV polarization results, provided initial volumetric images for inspection, corresponding maximum-intensity projections (MIPs) are presented in Figure 8, with the down-range direction in the positive  $y$ -axis direction. The 3D structure of the target and scene is evident. The shadowing to the rear of the model is not discernible due to the wide transmitter SAR aperture, however the shadow to the right of the vehicle, associated with the static receiver directions, is evident. The large sphere to the rear-right of the scene is marked “S”, and several associated multipath features are visible, one directly at ground level below the sphere, and the other symmetrically below ground level.

Having evaluated the incoherent sum result, a coherent sum of the nine bistatic 3D SAR image VV polarization results was performed. Coherent sums are however very sensitive to positional errors in SAR geometry information. It is estimated that a 4 mm range error in antenna ground truth, could give rise to as much as  $90^\circ$  of phase error at 10 GHz. Such a recorded error size would be possible in the laboratory antenna position ground-truth taking process in the directions perpendicular to the linear scanner actuators. (However, in the directions of the linear scanner actuators the accumulated positional errors after many thousands of moves were confirmed to be lower than 0.1 mm). Indeed, after forming an initial coherent sum the result was seen to be defocussed.

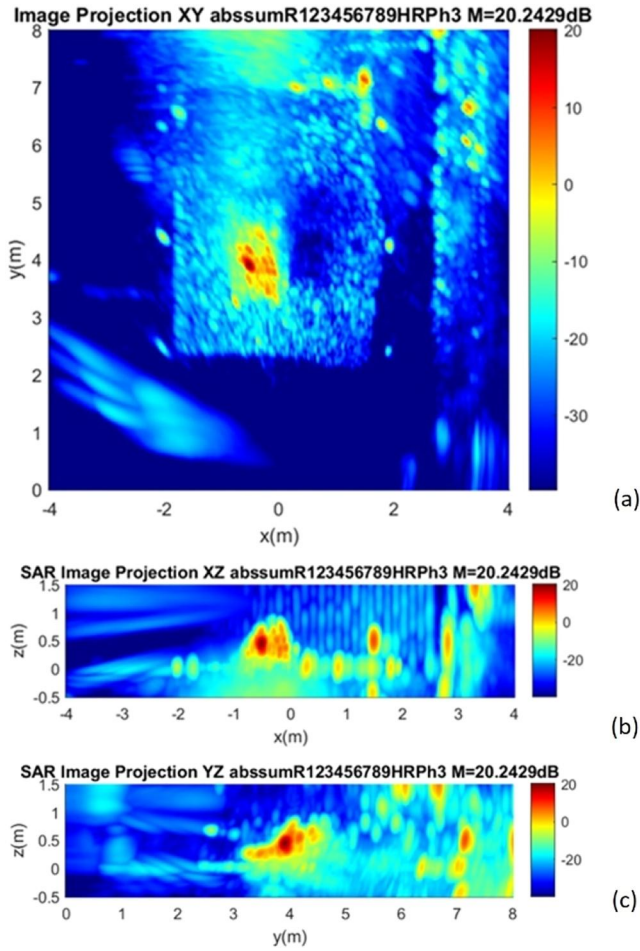


**FIGURE 8** MIPs of an incoherent sum of the nine VV polarization 3D bistatic SAR images, with a z-projection (a), y-projection (b), and an x-projection (c). The large reference sphere is marked “S”.

A data-driven phase correction algorithm was developed, maximising the intensity of the brightest scene scatterer in any given VV image pair coherent sum, providing an overall phase correction value for each of the nine bistatic SAR geometries. The result of the phase corrected nine VV polarization image coherent sum is presented in Figure 9, in the form of MIPs.

An improvement in SAR resolution in all three spatial dimensions has resulted from the phase corrected coherent summation, over the incoherent summation, providing finer detail across the main target and scene.

## 6.2 | Polarimetric decomposition of scene

The bistatic generalised Huynen decomposition has undergone previous evaluation with canonical scatterers, both in the literature [3] and in the GBSAR laboratory. In the current study, results for the complex scene are presented. The decomposition was applied to both the individual bistatic polarimetric images, and to the image sums. Volumetric SAR

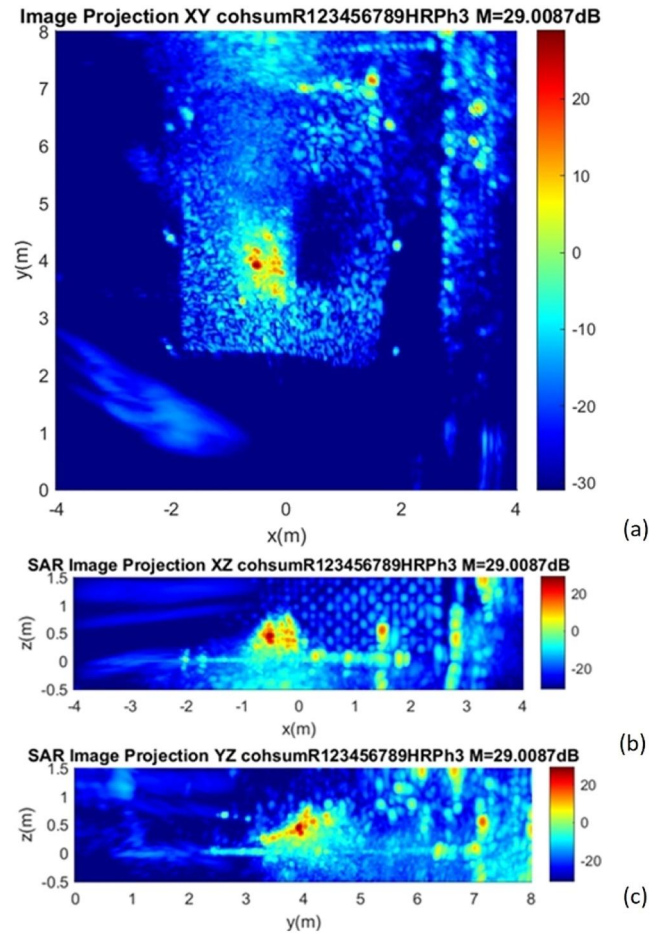


**FIGURE 9** MIPs of a phase corrected coherent sum of the nine VV polarization 3D bistatic SAR images, with a z-projections (a), y-projection (b), and an x-projection (c). The large reference sphere is marked “S”.

MIPs are presented for the phase corrected multistatic summed bistatic polarimetric images in Figures 10 and 11, with the pertaining colour maps shown in Figure 12, and selected features marked in the first and last images of the polarimetric set.

Note that for the SAR geometries investigated (seen in Figure 3), it was found that scatterers retained their polarimetric properties, both across the nine bistatic SAR geometries and in the phase corrected coherent sum. Only results from the coherent sum are presented here.

Firstly, the large reference sphere “S”, is behaving mostly as expected, with: low polarisability  $\gamma$  (green); Odd-bounce  $|\nu|$  (red); an unstable and meaningless set of orientations  $\theta_i$ ,  $\theta_s$  as expected; the symmetry  $|\tau_i|$ ,  $|\tau_s|$  values seem unstable however.

The T72 scale model shows a complex variety of scattering behaviour across it, and it is difficult to ascertain the origin of many features in MIP results alone, however some features are highlighted here.

The antenna wire on the model, marked “W” in the photographs in Figure 13, and in the MIPS in Figures 10 and 11, was tied down to the model body, and is consequently in

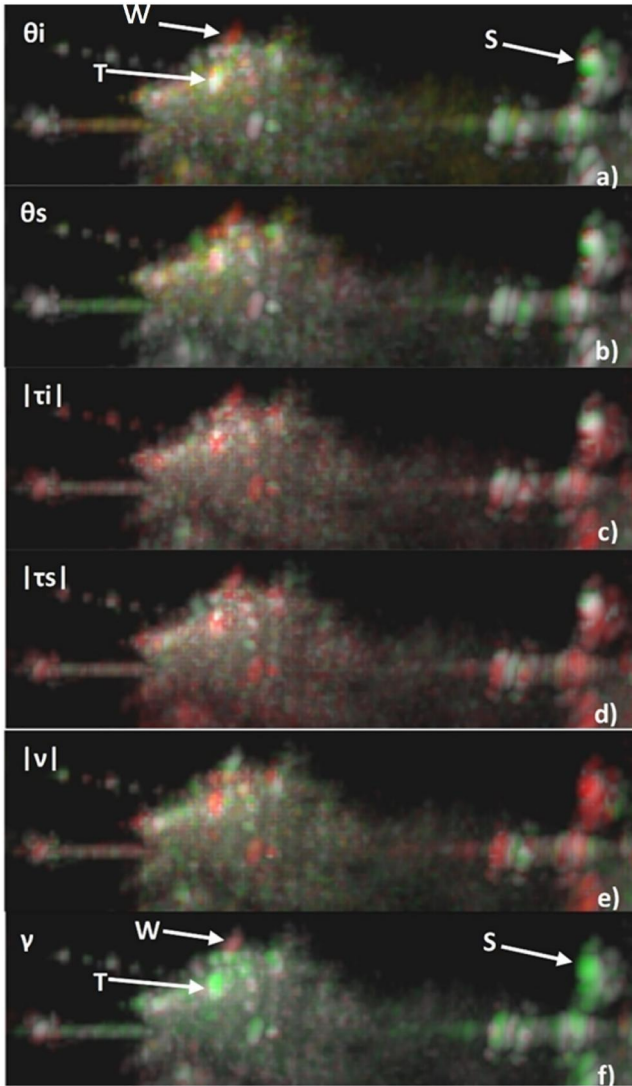


**FIGURE 10** Side-view Polarimetric decomposed MIPs showing  $\theta_i$ ,  $\theta_s$ ,  $|\tau_i|$ ,  $|\tau_s|$ ,  $|\nu|$ ,  $\gamma$  in (a) to (f) respectively, with colour maps presented in Figure 12.

the form of an arc. Parts of this component would be expected to behave as a dipole scatterer. This scatterer is behaving mostly as expected, with: high polarisability  $\gamma$  (red); orientations  $\theta_i$ ,  $\theta_s$  in the region of  $\sim 67^\circ$  (red-orange); high symmetry  $|\tau_i|$ ,  $|\tau_s|$  (red); however it is Even-bounce  $|\nu|$  (green).

A region on the side of the model T72 turret, marked “T” in Figure 13b), gives rise to a strong and stable specular scattering result in the bistatic SAR geometries. This concave surface specular scatterer is behaving as expected, with: low polarisability  $\gamma$  (green); Odd-bounce  $|\nu|$  (red); high symmetry  $|\tau_i|$ ,  $|\tau_s|$  (red); unstable and meaningless orientations  $\theta_i$ ,  $\theta_s$  as expected.

Other scatterers may be seen more clearly by rotating and slicing the polarimetric volumetric renderings within viewing software. The analysis of the results is ongoing and involves determining additional polarimetric data visualisation techniques.

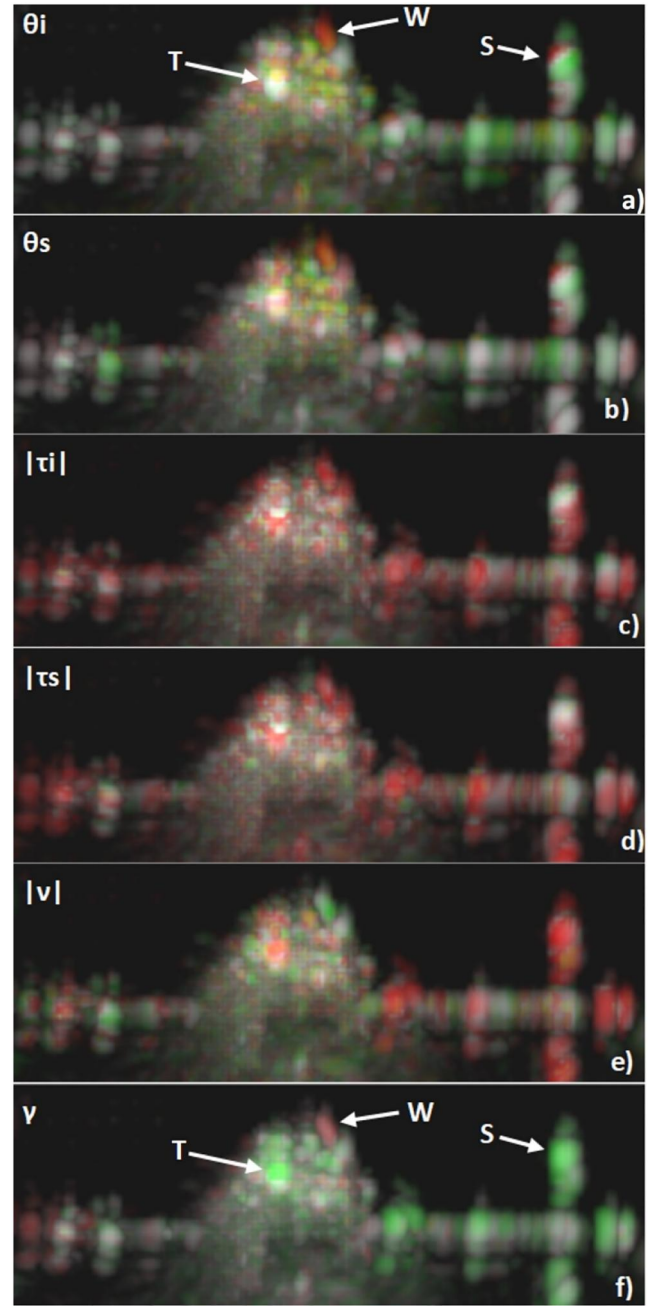


**FIGURE 11** Front-view polarimetric decomposed MIPs showing  $\theta_i$ ,  $\theta_s$ ,  $|\tau_i|$ ,  $|\tau_s|$ ,  $|\nu|$ ,  $\gamma$  in (a) to (f) respectively, with colour maps presented in Figure 12.

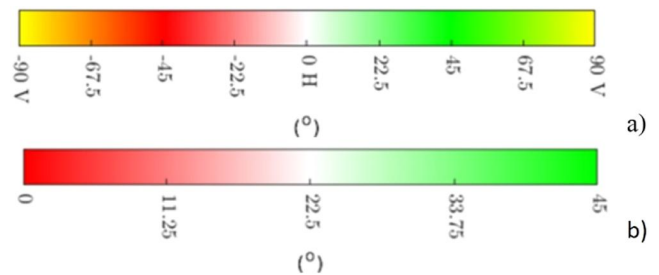


**FIGURE 12** Colour maps associated with Bistatic Huynen decomposition parameters  $\theta_i$ ,  $\theta_s$  (a) and  $|\tau_i|$ ,  $|\tau_s|$ ,  $|\nu|$ ,  $\gamma$  (b).



**FIGURE 13** Close-up side-views of the quarter scale T72 tank model. The highlighted parts are the arched antenna wire “W”, and the bistatic specular reflection point on the turret “T”.

## 7 | SPARSE APERTURE 3D POINT-CLOUD RESULTS

The SSARVI technique is applied to downsampled versions of the experimental dataset described in section 4, with the aim of determining a sub-Nyquist sampling limit for good quality results and determining effective ways of combining multistatic data from the different receivers when the scene consists of a complex target, as opposed to the idealised point scatterer investigated in Section 5. The results are shown for the four measured polarisation channels, to determine their utility.

Figure 14 shows the repeated random downsampling implemented for the transmitter aperture in the vertical direction, with the original aperture being presented in Figure 3. To provide an unambiguous vertical image extent across a 1.8 m high Volume of Interest (VoI), a conventional bistatic BPA based imaging approach would require a transmitter spacing of 7.8 cm between transmitter passes for the measured frequencies. For each method of receiver-data combination, passes were sequentially removed until the tank structure became indistinguishable from erroneous detection artefacts.

A threshold was determined for the tank structure using a subset of the geometry shown in Figure 3. Using a single receiver position, interferogram phase factors from all transmitter passes were summed forming a combined volumetric interferogram (the phase factor sum is always divided by the number of elements in sum, hence giving a mean). Background artefacts were then reduced by systematically increasing the

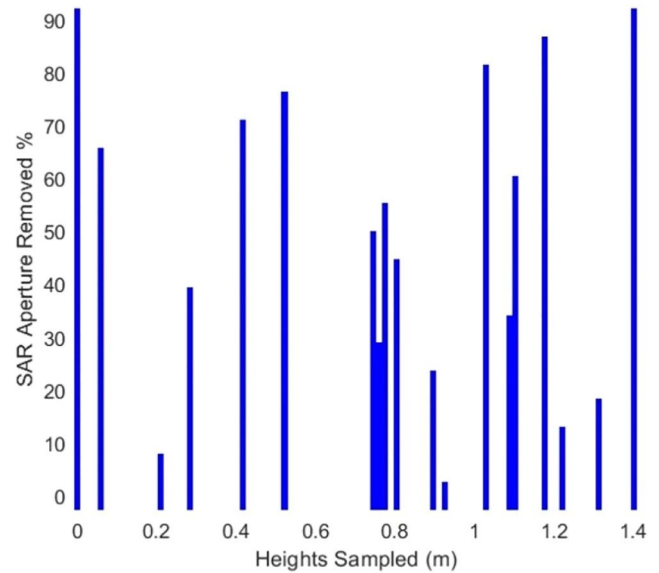


**FIGURE 14** Representation of the downsampled transmitter aperture. Blue lines show the transmitter height sampled, for a full aperture width, as a percentage of the initial transmitter aperture removed.

summed phase factor lower threshold. The threshold at which they were removed was determined to be optimal at the point which is 75% from the modal  $R$  value to the maximum  $R$  value across the whole VoI. This thresholding approach was maintained in the formation of the sub-Nyquist aperture point-cloud renderings, which enabled the appearance of artefacts to be associated with the performance of the SSARVI algorithm, providing the downsampling limits presented.

Figure 15 compares example sub-Nyquist point-cloud renderings formed from each of the three combination approaches described in Section 3, employing the VV linear polarisation data.

The renderings presented were formed using 10 randomly spaced transmitter passes, extracted from the radar geometry shown in Figure 3, employing receivers 3, 6, and 9, which are in a single vertical column. The resulting transmitter aperture had a mean pass spacing of 14.1 cm, which would give a maximum unambiguous vertical cross-range extent of 1.2 m when using conventional image formation. This sampling corresponds to 47% removal of data from the initial aperture seen in Figure 14.

From the point-cloud detections, the tank structure is clearly visible for all three methods of receiver combination, with the main body appearing the brightest. The cannon barrel is visible, and the gravel is visible. The point-cloud rendering shown in Figure 15c (“combined”) shows the most points detected out of the three methods, and the most discernible tank structure in the point-cloud formation. With the “summed” combination approaches, both coherent and non-coherent, there is a section of the rear body missing from the point-cloud rendering with the cannon also less well defined.

In determining the effect of removing passes from the transmitter aperture, a 3D cross correlation was performed

between consecutive sub-Nyquist formed point-cloud renderings and the initial sampling point-cloud rendering. The cross-correlation measures similarity between two 3D point-clouds, represented as 3D images. The point-cloud renderings formed with the initial sampling rate were free of erroneous detections, therefore significant decreases in correlation with aperture downsampling can be reasonably attributed to the appearance of erroneous detection artefacts. Sections 7.1–7.3 present the results with this measure, for each receiver combination method, to highlight trends in image quality.

The correlation results are compared to the point-clouds themselves by a process of direct visual inspection, for each sparse aperture employed. The direct inspection process was used to determine the aperture downsampling limits for the cases:

- (1) where only minor artefacts are present, and
- (2) where major but not overwhelming artefacts are present.

The case of “major but not overwhelming artefacts” is included as these renderings are deemed to still provide useful results, as the target can still be discerned. Beyond this point however, the target is no longer discernible. The two sparse

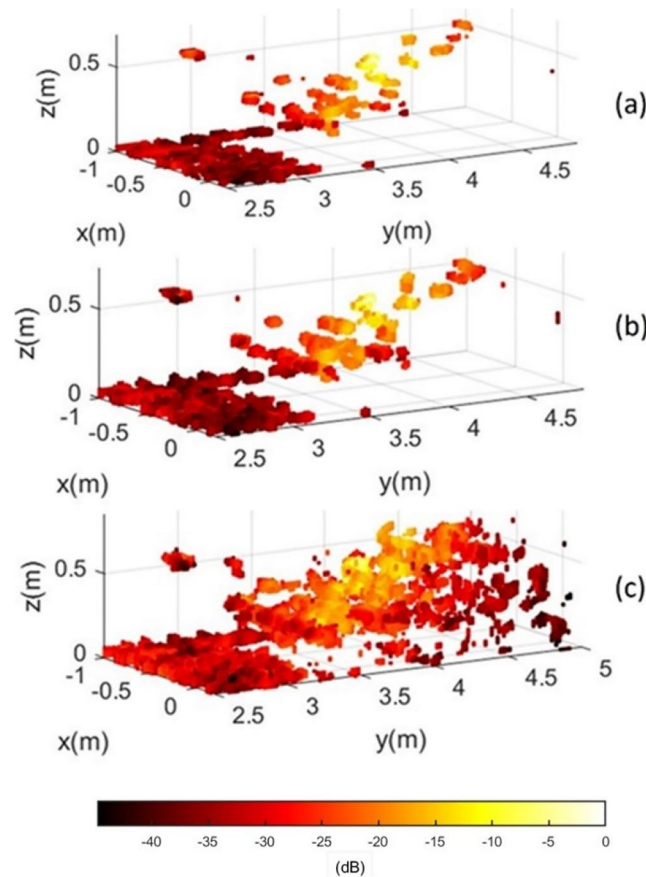


**FIGURE 15** VV polarisation measurement sub-Nyquist transmitter height sampled multistatic point-cloud renderings. (a) Coherently summed, (b) Non-coherent bistatic summed, and (c) Non-coherent bistatic combined.

aperture downsampling limits for point-cloud formation are summarised in Table 1 for the different polarisations and receiver data combination methods.

To determine the effect of using increasing amounts of receiver aperture data (increasing fixed receiver positions), the maximum summed phase factor value,  $R$ , for the brightest scatterer in the scene is presented, for the different polarisations and multistatic data combination approaches, in Sections 7.1–7.3. The receiver positions used are those shown in Figure 3, with the full width of receivers spanning a total width of  $18.6^\circ$  in azimuth, and  $17.0^\circ$  in elevation.

## 7.1 | Coherent multistatic summation

Figure 16 shows the downsampling aperture point-cloud correlation performance for the *coherent* multistatic summed approach, for the four polarisations against their corresponding initial sampling point-cloud rendering. The receiver column employed in generating the Figure 15 results (receivers 3, 6, 9)

**TABLE 1** Table showing the aperture downsampling limits for point-clouds with minor and major artefacts, for all three receiver combination approaches: coherent multistatic sum (CMS), non-Coherent multistatic sum (NCMS), and non-coherent bistatic combination (BC).

Pol.	Downsampling limit for only minor artefacts (%)			Downsampling limit for only major artefacts (%)		
	CMS	NCMS	BC	CMS	NCMS	BC
HH	74	68	32	78	73	57
HV	74	68	42	78	73	57
VH	74	68	36	78	78	57
VV	74	68	42	78	73	57

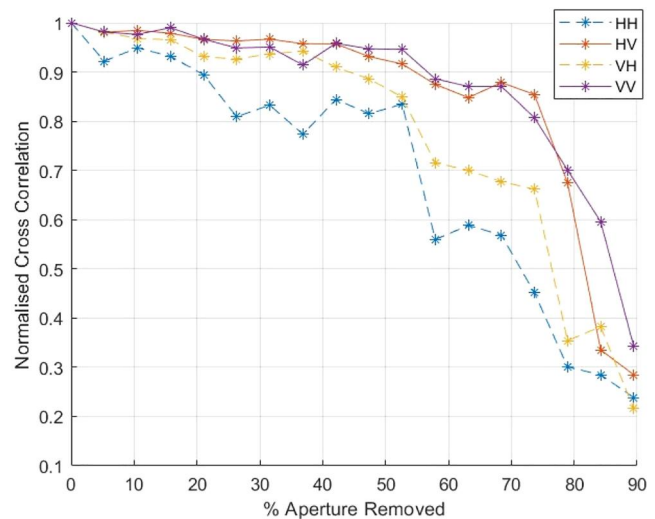


**FIGURE 16** Normalised cross-correlation between successive coherent summed bistatic sparse aperture point-cloud renderings and the corresponding initial-sampling point-cloud renderings for each polarization.

were used in generating subsequent multistatic point-cloud correlation results.

The correlation values necessarily start at 1 for all polarisations, and then show a decline as passes were removed from the aperture. For the VV and HV channels, the correlation remained above 0.8 until 74% of the original aperture had been removed. Inspection of the point-cloud renderings indicated that this corresponds to sparse apertures for which only a small number of erroneous detections were present. Although the correlation values for the remaining polarisations were lower, inspection of point-clouds showed consistency across all polarisations for given aperture sparsity. Hence the correlation values should be taken to represent trends rather than exact point-cloud detection performance.

The correlation then showed a rapid decline, so that up until 78% aperture removal there were major but not overwhelming erroneous detections. Beyond the 78% aperture removal, the target is overwhelmed by image artefacts so that no useful target information is obtained. The aperture downsampling limit values are provided in Table 1.

To illustrate the effect of adding measured data from an increasing number of receivers, Figure 17 shows the summed phase factor,  $R$ , at the location of the brightest scatterer in the scene for each polarisation. This scatterer was located on the vehicle turret and is labelled in Figure 13. The values of  $R$ , for the three multistatic combination methods, were generated using an increasing number of receivers, with a fixed transmitter aperture. The transmitter aperture consisted of 14 passes, corresponding to 26% initial aperture removal. The first three receiver positions plotted, correspond to those used to form the renderings and correlation results shown in Figures 15 and 16.

Most of the polarisations initially show a pronounced decrease in  $R$ , which then became less pronounced. Direct inspection of point-clouds revealed that the decrease was associated with a decrease in the number of detections. This

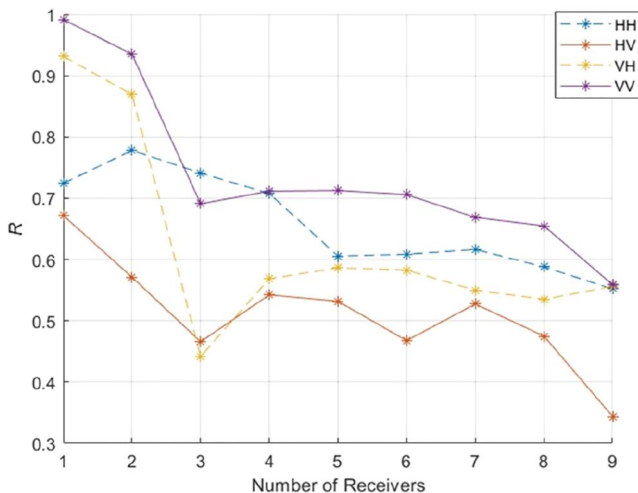


**FIGURE 17** Summed phase factor response when coherently summing data from an increasing number of receivers, for the brightest scatterer in each polarisation.

decrease in complex phase factor sum is likely associated with the scatterer variability in bistatic complex RCS. The isotropic point scatterer simulation results in Figure 6 showed no such decrease in  $R$ .

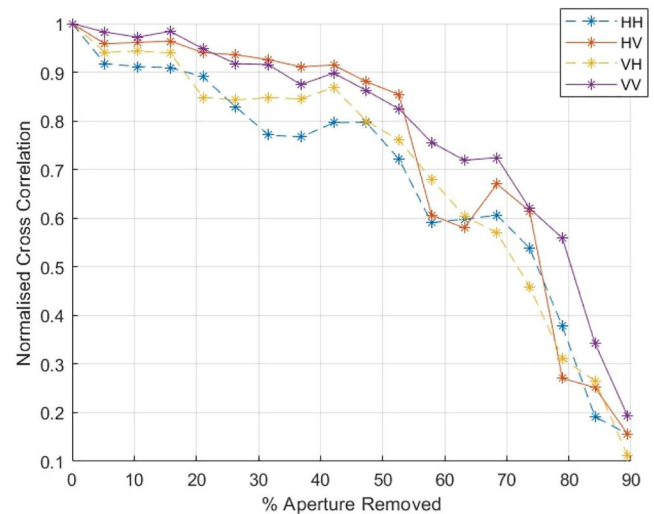
## 7.2 | Non-coherent multistatic summation

Figure 18 shows the downsampling aperture point-cloud correlation performance for the non-coherent multistatic summed approach, for the four polarisations against their corresponding initial sampling point-cloud rendering, and the same geometries as in Section 7.1.

The correlation values mostly remain above 0.8 until 47% of the initial aperture is removed, after which they show a faster decline. Point-cloud inspection revealed that only minor artefacts were present until 68% of the initial aperture was removed. This aperture downsampling point occurred earlier than in the coherently summed approach. The last usefully interpretable point-cloud renderings, where ‘major but not overwhelming’ artefacts are present, occurred when 73% of the initial sampled aperture was removed. The downsampling values are summarised in Table 1.

For the non-coherent multistatic summation, to illustrate the effect of adding measured data from an increasing number of receivers, Figure 19 shows the summed phase factor,  $R$ , at the location of the brightest scatterer in the scene for each polarisation. This scatterer was located on the vehicle turret and is labelled in Figure 13, and the conditions for the generation of the results were as in the corresponding ones in Section 7.1.

Most of the polarisations initially show a decrease in  $R$ , after which they then mostly stabilise and, in some cases, increase slightly. Likely due to this trend, when comparing the corresponding point-clouds with the coherent summed



**FIGURE 18** Normalised cross-correlation between successive non-coherent summed bistatic sparse aperture point-cloud renderings and the corresponding initial-sampling point-cloud renderings for each polarisation.

approach point-clouds, more detections were visible in the non-coherent summation case. The additional detections are distributed across the main body of the vehicle. It is likely that this property comes about due to the reduced sensitivity of the non-coherent multistatic addition approach to the RCS variation between bistatic geometries. The reduced sensitivity, however, has led to lower aperture removal limits when compared to the coherent summation case, as seen in Table 1.

### 7.3 | Non-coherent combined bistatic

Figure 20 shows the downsampling aperture point-cloud correlation performance for the *non-coherent combined* bistatic approach, for the four polarisations against their corresponding

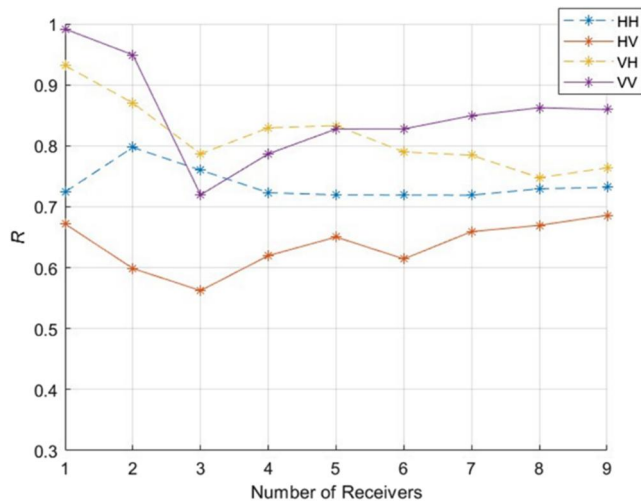


FIGURE 19 Maximum summed phase factor value when non-coherently summing data from an increasing number of receivers.

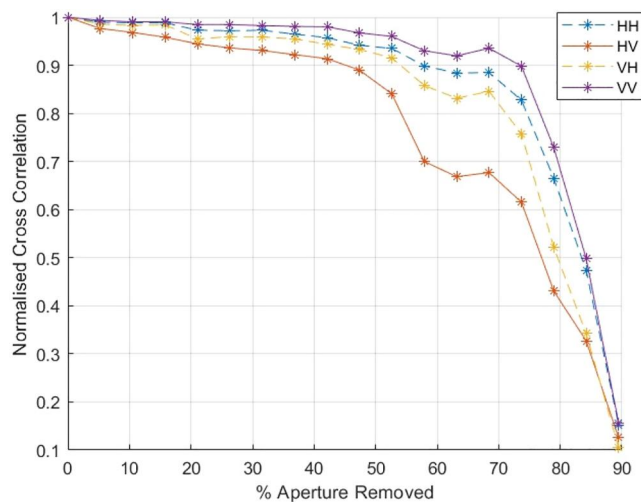


FIGURE 20 Normalised cross-correlation between successive non-coherent combined bistatic sparse aperture point-cloud renderings and the corresponding initial-sampling point-cloud renderings for each polarization.

initial sampling point-cloud rendering, and the same geometries as in Section 7.1.

The downsampled aperture point-cloud correlation curves are smooth and relatively high valued in comparison to the summed approaches, however more artefacts were present. Only minor artefacts were present up until between 32% and 42% depending on the polarisation, and major artefacts were introduced at 57%, both earlier limits than in the summation approaches (Sections 7.1, 7.2). These limits are shown in Table 1. Generally, the combination approach showed significantly more initial detections and a more complete initial vehicle structure. Example point-clouds were presented in Figure 15, illustrating this.

It is seen that with the combination approach, for a given transmitter aperture, incorporating an increasing number of receivers adds further detections. This is in contrast with the previous two approaches, which both showed a decrease in the number of detections as receivers were added. This approach is the least sensitive to variations in bistatic RCS however, it generally requires more passes than the summation approaches due to the faster onset of erroneous detections.

### 7.4 | Point-cloud properties summary and polarimetric results

This section compares the point-clouds of the three multistatic summation approaches for the four polarisations and summarises some of the properties observed for the various point-cloud results.

The point-cloud sparse aperture artefact limits for minor and major artefacts, are presented in Table 1. Regarding false scatterer artefacts, for a given aperture sparsity, the coherent summation gives the least, followed by the non-coherent summation and then the non-coherent combination approach. Similarly, it was observed that for a given aperture sparsity where little or no false scatterers were present, the coherent summation approach gave the fewest scatterer detections over the vehicle, followed by the non-coherent summation and then by the non-coherent combination, as seen in the example results in Figure 15.

Regarding the point-clouds formed in the different polarimetric channels for a given multistatic SAR geometry and combination approach, it was found that the actual detections differed across the channels. Figure 21 shows this for the three-receiver scenario with 26% of passes removed from the transmit aperture, by overlaying the four point-clouds in a single plot with different colours for different polarisations. It is noted that the SSARVI algorithm and thresholding process was applied to the channels separately.

The result shows that each polarisation contributes a significant amount of different scatterer detections, so that when they are combined, a more complete outline of the vehicle is provided. Of the three multistatic combination approaches, the coherent summation one benefits most from the overlay of the polarimetric channels as for any given aperture it has the least detections.

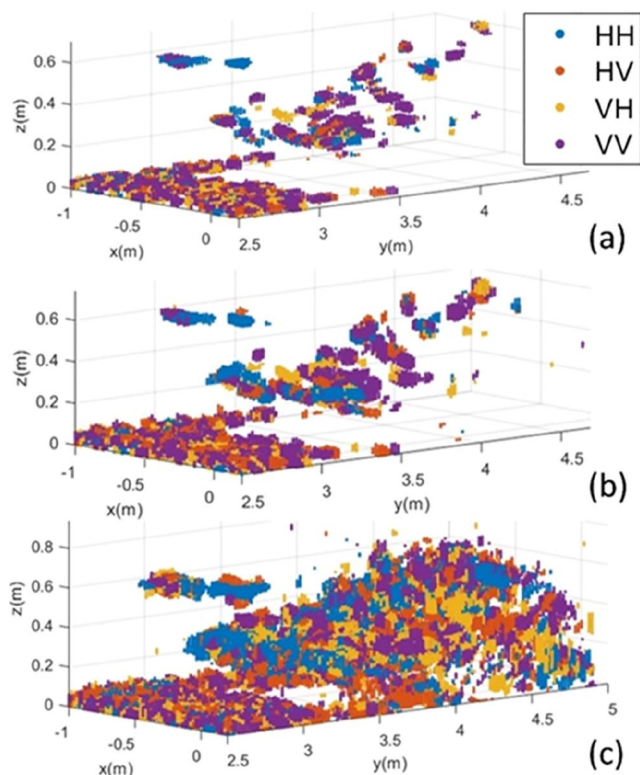


**FIGURE 21** Overlaid point-clouds from each polarisation channel, shown for the three multistatic geometry combination methods: (a) Coherent summation, (b) Non-coherent bistatic summed, and (c) Non-coherent bistatic combined.

## 8 | CONCLUSION

Multistatic polarimetric SAR measurements of a complex target and scene were conducted at the Cranfield University GBSAR laboratory, to determine benefits of these type of collection geometries.

Results have been presented which combine multiple bistatic SAR collections to provide 3D SAR (volumetric) images of the scene. Full Nyquist sampled measured data were collected and image processed with the back-projection image formation algorithm (BPA), and downsampled versions of the collected data were processed with the novel, and here extended to multistatic SAR geometries, sparse aperture point-cloud formation algorithm, SSARVI.

For the Nyquist sampled datasets, incoherent summation of the individual bistatic collections provides useful BPA derived results, allowing a clear determination of the target, however with the SAR geometries utilised, a phase corrected coherent summation of the nine bistatic SAR collections was shown to provide BPA results with a much-improved SAR resolution in all three spatial dimensions.

A bistatic generalised Huynen polarimetric decomposition was applied to the data, and for the SAR geometries investigated, it was found that scatterers retained their polarimetric properties, both across the nine bistatic SAR geometries and in the phase corrected coherent sum.

Maximum intensity BPA image projections were presented, and specific scatterers were highlighted, along with their scattering polarimetric characteristics.

A multistatic SAR geometries extension of the SSARVI approach for generating sub-Nyquist SAR aperture 3D point-cloud renderings [19] was presented. With simulations, it was shown that excessive clustering of trajectories can reduce the sidelobe performance substantially, essentially due to multiple trajectories behaving as a single trajectory. When designing non-even trajectories for collections, trajectory cluster extents below the Nyquist spacing are suboptimal, as the advantages of having the clustered multiple trajectories are then lost. With a generalised bistatic example, it was shown that for a given desired unambiguous vertical cross-range extent, the extent of clustered trajectories should not be finer than approximately two times the corresponding Nyquist sample spacing, otherwise the trajectory distribution becomes sub-optimal.

A comparison of three different methods for combing the multistatic data from different receivers was made. Out of the three approaches implemented, it was found that coherent summation of the data was the most effective approach to suppressing artefact detections but gave rise to fewest point-cloud detections overall. The non-coherent summing approach showed similar results but with more detections and more artefacts for any given sparse SAR aperture. Overlaying the detections in the ‘Non-coherent Bistatic Combined’ approach gave rise to the most detections but required more passes for suppressing higher levels of detection artefacts.

For the coherent and non-coherent summed methods, it was found that increasing the number of receiver datasets used for point-cloud formation resulted in a drop in the number of points detected. The “non-coherent bistatic combined” approach led to the most complete outline of the target but contained the most artefact detections. These different approach behaviours are likely due to their varying sensitivity to the variation in bistatic RCS across the different receiver datasets.

It was found that each polarisation channel contributes a significant amount of different scatterer detections, so that when they are combined, a more complete outline of the vehicle is provided. Of the three multistatic combination approaches, the coherent summation one benefits most from the overlay of the polarimetric channels as for any given aperture it has the least detections.

Further research will include developing the SSARVI approach for polarimetric decompositions other than the linear set, to provide a polarimetric characterisation of detections. Further effects expected in realistic conditions should also be considered, such as SAR geometry errors, noise, and target motion. It is possible that different summed phase factor thresholds might be appropriate for different scenes. Potentially electromagnetic scattering simulation could allow the generation of target specific thresholds [11].

## AUTHOR CONTRIBUTIONS

**Richard Welsh:** Conceptualization; data curation; formal analysis; investigation; methodology; software; validation; visualization; writing – original draft; writing – review &

editing. **Daniel Andre:** Conceptualization; data curation; formal analysis; funding acquisition; investigation; methodology; project administration; software; supervision; validation; visualization; writing – review & editing. **Mark Finnis:** Resources; software.

## ACKNOWLEDGEMENTS

This investigation was sponsored by the Defence Science and Technology Laboratory (DSTL).

## CONFLICT OF INTEREST STATEMENT

The authors declare no conflicts of interest.

## DATA AVAILABILITY STATEMENT

SAR data are the subject of ongoing research but may be made available on request to the author or the Cranfield GBSAR group.

## ORCID

Richard Welsh  <https://orcid.org/0000-0003-1111-8840>

Daniel Andre  <https://orcid.org/0000-0001-5523-446X>

## REFERENCES

- Horne, A., et al.: Exploration of Multidimensional Radio Frequency Imaging to Derive Remote Intelligence of Building Interiors (2018)
- Kuang, H., et al.: Fully three-dimensional UAV SAR imaging with multi-azimuth angle observation. In: IEEE International Geoscience and Remote Sensing Symposium (2017)
- Titin-Schnaider, C.: Physical meaning of bistatic polarimetric parameters. *IEEE Trans. Geosci. Rem. Sens.* 48(5), 2349–2356 (2010). <https://doi.org/10.1109/tgrs.2009.2038063>
- Titin-Schnaider, C.: Characterization and recognition of bistatic polarimetric mechanisms. *IEEE Trans. Geosci. Rem. Sens.* 51(3), 1755–1774 (2013). <https://doi.org/10.1109/tgrs.2012.2208118>
- Titin-Schnaider, C.: Polarimetric Characterization of bistatic coherent mechanisms. *IEEE Trans. Geosci. Rem. Sens.* 46(5), 1535–1546 (2008). <https://doi.org/10.1109/tgrs.2008.916078>
- Elgy, J., Andre, D., Finnis, M.: Volumetric SAR near-field upsampling and basebanding. *Electron. Lett.* 56(12), 622–624 (2020). <https://doi.org/10.1049/el.2019.4123>
- Austin, C.D., Ertin, E., Moses, R.L.: Sparse multipass 3D SAR imaging: applications to the GOTCHA data set. In: *Proc. SPIE 7337, Algorithms for Synthetic Aperture Radar Imagery XVI* (2009)
- Moreira, A., et al.: A tutorial on synthetic aperture radar. *IEEE Geosci. Rem. Sens. Mag.* 1(1), 6–43 (2013). <https://doi.org/10.1109/mgrs.2013.2248301>
- Xu, G., et al.: Sparse synthetic aperture radar imaging from compressed sensing and machine learning: theories, applications, and trends. *IEEE Geosci. Rem. Sens. Mag.* 10(4), 32–69 (2022). <https://doi.org/10.1109/mgrs.2022.3218801>
- Carnade, R., Cohen, D.: “SAR Point Cloud Generation System”. USA Patent US9417323B2 (2014)
- Wollard, M., et al.: SARCASTIC v2.0—high-performance SAR simulation for next-generation ATR systems. *J. Rem. Sens.* 14(11), 2561 (2022). <https://doi.org/10.3390/rs14112561>
- Manzoor, Z., Qaseer, M., Donnel, K.: Image distortion characterization due to equivalent monostatic approximation in near-field bistatic SAR imaging. *IEEE Trans. Instrum. Meas.* 69(7), 4898–4907 (2020). <https://doi.org/10.1109/tim.2019.2957868>
- Zeng, T., Cherniakov, M., Long, T.: Generalized approach to resolution analysis in BSAR. *IEEE Trans. Aero. Electron. Syst.* 41(2), 461–474 (2005). <https://doi.org/10.1109/taes.2005.1468741>
- Rambour, C., et al.: From interferometric to tomographic SAR. *IEEE Geosci. Rem. Sens. Mag.* 8(2), 6–29 (2020). <https://doi.org/10.1109/mgrs.2019.2957215>
- He, T., et al.: Airborne sparse flight array SAR 3D imaging based on compressed sensing in frequency domain. *J. Syst. Eng. Electron.* 34(1), 56–67 (2023). <https://doi.org/10.23919/jsee.2022.000125>
- Ren, H., et al.: Swarm UAV SAR for 3-D imaging: system analysis and sensing matrix design. *IEEE Trans. Geosci. Rem. Sens.* 60, 1–16 (2022). <https://doi.org/10.1109/tgrs.2022.3221775>
- Corbett, B., Andre, D., Finnis, M.: Localising vibrating scatterer phenomena in synthetic aperture radar imagery. *Electron. Lett.* 56(8), 395–398 (2020). <https://doi.org/10.1049/el.2019.4114>
- Huynen, J.: *Phenomenological Theory of Radar Targets*. TU Delft (1970)
- Welsh, R., Andre, D., Finnis, M.: Volumetric interferometry for sparse 3D synthetic aperture radar with bistatic geometries. *Electron. Lett.* 59(12) (2023). <https://doi.org/10.1049/el.2023.12851>
- Andre, D., Morrison, K.: A volumetric approach to SAR interferometry. In: *Proceedings of the Institute of Acoustics* (2014)
- Budillon, A., Evangelista, A., Schirrinzi, G.: Three-dimensional SAR focusing from multipass signals using compressive sampling. *IEEE Trans. Geosci. Rem. Sens.* 49(1 PART 2), 488–499 (2011). <https://doi.org/10.1109/tgrs.2010.2054099>
- Russ, J.C., Neal, F.B.: *The Image Processing Handbook*, 7th ed, pp. 1–1032 (2016)
- Zebker, H.A., Vilasenor, J.: Decorrelation in interferometric radar echoes. *IEEE Trans. Geosci. Rem. Sens.* 30(5), 950–959 (1992). <https://doi.org/10.1109/36.175330>
- Gao, G., et al.: Onboard information fusion for multisatellite collaborative observation. *IEEE Geosci. Rem. Sens. Mag.* 11(2), 40–59 (2023). <https://doi.org/10.1109/mgrs.2023.3274301>
- Krieger, G., et al.: Interferometric synthetic aperture radar (SAR) missions employing formation flying. *Proc. IEEE* 98(5), 816–843 (2010). <https://doi.org/10.1109/jproc.2009.2038948>
- Minh, D.H.T., Tebaldini, S.: Interferometric phase linking. *IEEE Geosci. Rem. Sens. Mag.* 11(3), 46–62 (2023). <https://doi.org/10.1109/mgrs.2023.3300974>

**How to cite this article:** Welsh, R., Andre, D., Finnis, M.: Laboratory multistatic 3D SAR with polarimetry and sparse aperture sampling. *IET Radar Sonar Navig.* 1–14 (2024). <https://doi.org/10.1049/rsn2.12528>